PERGAMON

International Journal of Heat and Mass Transfer 46 (2003) 283–296

International Journal of HEAT and MASS TRANSFER

www.elsevier.com/locate/ijhmt

Effects of gravity and ambient pressure on liquid fuel droplet evaporation

George Gogos *, Siang Soh, Daniel N. Pope

Department of Mechanical Engineering, University of Nebraska-Lincoln, N104 Walter Scott Engineering Center, Lincoln, Nebraska 68588-0656, USA

Received 11 July 2000; received in revised form 7 July 2002

Abstract

An axisymmetric numerical model has been developed to conduct a study of single droplet evaporation over a wide range of ambient pressures both under normal and microgravity conditions. Results for droplet lifetime as a function of ambient pressure and initial droplet diameter are presented. The enhancement in the droplet evaporation rate due to natural convection is predicted. This enhancement becomes more dominant with increasing ambient pressure due to the increase in the Grashof number. The higher the ambient pressure, the closer the Grashof number remains to its initial value throughout most of the droplet lifetime because of the droplet swelling and the heat-up of the droplet interior. Results should be particularly of interest to researchers conducting experiments on droplet evaporation at elevated pressures within a normal gravity environment. The model developed is in good agreement with experimental data at low pressures. Explanations have been provided for its deviation at high pressures.

1. Introduction

Droplet evaporation is an important process in many devices, such as diesel engines, liquid–fuel rocket engines, aircraft jet engines and industrial furnaces. During spray combustion in such devices, fuel droplets are injected into the combustion chamber in liquid form and most of the droplets evaporate before combustion takes place. The concentration of the fuel vapor is determined by the rate of evaporation of the droplets and it affects the performance of the combustion system significantly [1]. In order to improve thermal efficiency, the operating pressures of these devices are in general near or above the critical pressure of the fuel.

The literature on droplet evaporation at elevated pressures has become quite extensive, especially over the last decade. It has been recently reviewed by Givler and Abraham [2], Sirignano [3] and Bellan [4]. These reviews indicate that only a few studies have attempted modeling of droplets within convective flows under high pressure conditions. Lee et al. [5] modeled dispersion of a vapor fuel droplet that is suddenly set in motion in a gaseous environment that has a density similar to that of the fuel vapor. The objective of the study was to describe the mixing and deformation process encountered by a supercritically preheated fuel droplet that is suddenly injected in a gaseous environment that is well above the thermodynamic critical temperature and pressure of the fuel. Results obtained show that the initially spherical gaseous fuel droplet is extensively distorted, adopting a mushroom-like shape.

Litchford and Jeng [6], and Delplanque and Sirignano [7] included convection in their models for liquid oxygen (LOX) droplet vaporization at elevated pressures by using film models. Delplanque and Sirignano [7] showed that stripping (mass removal from the droplet surface due to aerodynamic shearing) was likely to occur in typical rocket engine environments. Delplanque and Sirignano [8] developed an integral analysis of the coupled gas–liquid boundary layer at the droplet interface and obtained an expression for the mass removal rate

* Corresponding author. Tel.: +1-402-472-3006; fax: +1-402-472-1465.

E-mail address: ggogos@unl.edu (G. Gogos).

0017-9310/03/$ - see front matter
PII: S0017-9310(02)00269-7

Nomenclature

a, b	parameters in Peng–Robinson equation of state
c_p	specific heat capacity at constant pressure
d	diameter of the droplet
D_{12}	binary mass diffusion coefficient
g	gravitational acceleration
Gr	Grashof number $(Gr = (\bar{\rho}_s - \rho_\infty)R^3 g/\rho_\infty \nu_\infty^2)$
h	specific enthalpy
k	thermal conductivity
K	droplet evaporation constant
$\dot{m}''$	mass flux at the droplet interface
P	pressure
r	spherical radial coordinate
R	radius of the droplet
$\dot{R}$	droplet surface regression rate
R_u	universal gas constant
Re	Reynolds number
r_∞	outer computational boundary
t	time
t_e	droplet lifetime
T	temperature
$\vec{V}$	velocity vector
V_r	radial velocity
V_θ	polar velocity
Y	mass fraction of species
z	radial transformation coordinate

Greek symbols

α	thermal diffusivity
θ	spherical polar coordinate
μ	absolute viscosity
ν	kinematic viscosity
ϕ	azimuthal coordinate
ρ	density
τ	stress tensor

Subscripts

1	the liquid fuel species
2	the inert gas
d	motion pressure
g	gas phase
l	liquid phase
0	initial variable
r	radial variable
s	surface variable
∞	ambient variable
θ	polar variable

Superscripts

$-$	average value
$'$	gas phase dimensionless parameter
$''$	liquid phase dimensionless parameter

due to stripping, including blowing effects. The above mentioned studies have provided invaluable insight on convective effects, and secondary atomization [8], at elevated pressures. However, the lack of experimental data under the strong convective conditions considered in all these studies prevents a thorough validation of the theories developed.

The goal of the present study is to develop an experimentally validated numerical model that can simulate droplets evaporating within convective flows under high pressure conditions. Of particular relevance to this study are well characterized experimental studies on droplet evaporation at elevated pressures within a normal gravity environment. Matlosz et al. [9] investigated the evaporation of a *n*-hexane single droplet over a wide range of ambient pressures within a normal gravity environment. Their study showed that droplet lifetime decreases with increasing ambient pressure. Recently, Nomura et al. [10] conducted extensive experiments on the evaporation of a *n*-heptane droplet at various ambient temperatures and pressures under normal and under microgravity conditions. Their results clearly show that the effect of natural convection is significant. Admittedly, the convective fields due to buoyancy in these experiments are weak compared to the significant relative velocity between the gas and the droplet that exists in practical environments [3]. However, an experimentally validated numerical model that includes an environment that is both convective and at high pressure is a significant first step.

A comprehensive axisymmetric transient model which includes high pressure effects, gas and liquid phase variable properties, and liquid phase internal circulation has been developed. Both experimental studies mentioned above have been used for model validation. Furthermore, ambient pressure, initial droplet diameter and gravitational acceleration are varied to determine their effects on quantities of interest. Results should be particularly of interest to researchers conducting experiments on droplet evaporation at elevated pressures within a normal gravity environment. Preliminary results have been discussed in [11,12].

2. Problem description

Consider a cold liquid fuel droplet of initial radius (R_0) and temperature (T_0) evaporating into a hot and

initially stagnant inert environment of infinite expanse. The ambient pressure, temperature and mass fraction of the fuel vapor are prescribed as P_∞, T_∞, and $Y_{1,\infty}$, respectively. The droplet is stationary at all times and it initially consists of a single chemical component.

Soon after the droplet is introduced into the hot environment, a buoyancy-induced, downward moving, external flow field is formed near the droplet surface due to a density gradient which arises in response to the temperature difference between the droplet surface and the gaseous surroundings. The flow field is laminar, axisymmetric and it is coupled with the radial flow field that is induced by droplet evaporation. The shear stress exerted by this buoyancy-induced external flow at the liquid/gas interface causes an internal circulation in the liquid phase.

The liquid droplet is initially at a uniform temperature. Energy is transferred from the gas phase to the liquid phase. Part of the energy is used to heat-up the interior of the liquid droplet, while the rest is used for droplet evaporation. At high pressures, the ambient gas dissolves into the liquid droplet. At the droplet interface, thermodynamic vapor-liquid equilibrium is reached. The evaporation of the fuel droplet results in a decrease of droplet radius. The evaporating fuel is diffused and convected away from the droplet surface and the gas phase becomes a mixture of fuel vapor and ambient gas.

The physical geometry of the problem is illustrated in Fig. 1 where V_r is the radial velocity, V_θ is the polar velocity, r is the radial coordinate starting from the center of the droplet, and the polar coordinate θ is measured clockwise starting from the vertical axis.

In the present study, a *n*-hexane or *n*-heptane fuel droplet evaporating in a nitrogen environment is considered. An axisymmetric numerical model has been developed which includes high pressure effects, such as non-ideal gas phase behavior, the real gas effect on the heat of vaporization, the real gas effect on the vapor–liquid equilibrium at the droplet interface, solubility of ambient inert species into the liquid phase, the transient character of the gas and the liquid phase, and gas and liquid phase variable properties. The model also considers the liquid phase internal circulation caused by the shear stress at the droplet surface. Changes in the liquid phase density due to both thermal expansion and change in species composition contribute to the rate at which the droplet surface is receding and are incorporated in the model.

The assumptions employed in the current study are:

1. The droplet shape remains spherical, since the Weber number is mostly small. However, at elevated ambient pressures, the droplet may experience considerable deformation as a result of the decreased surface tension. This deformation is not considered in the present study.
2. Viscous dissipation and compressibility effects in the energy equation are neglected, since the relevant Mach number is negligibly small.
3. Radiation is negligible.

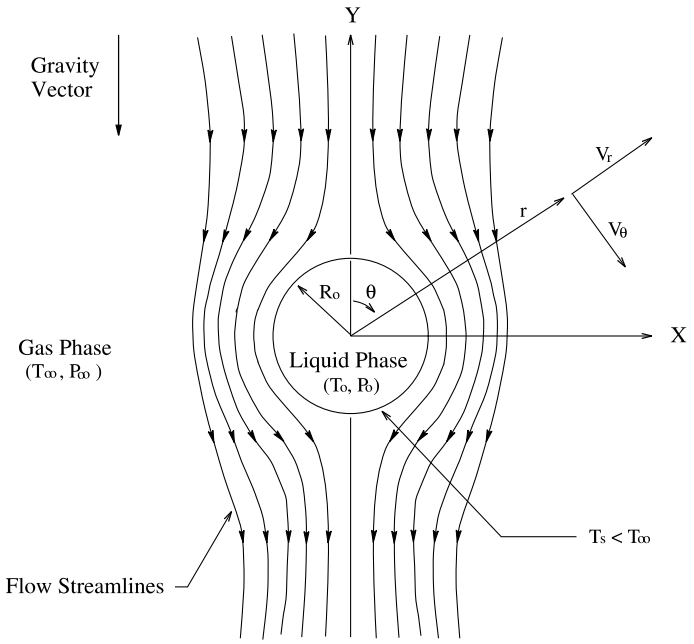

Fig. 1. A stationary cold liquid fuel droplet evaporating within a hot gas environment.

4. Second order effects such as the Soret and Dufour effects are negligible.
5. There are no heat/mass sources or chemical activity.

3. Governing equations

The momentum, heat and mass transfer processes are studied by solving the governing conservation equations in the gas and liquid phase which are coupled via the interface equations. Based on the above assumptions, the governing equations for both the gas and liquid phase in spherical coordinates are:

Conservation of mass

$$\frac{\partial \rho}{\partial t}+\frac{1}{r^2}\frac{\partial}{\partial r}(\rho r^2 V_r)+\frac{1}{r\sin\theta}\frac{\partial}{\partial \theta}(\rho V_\theta \sin\theta)=0 \tag{1}$$

Conservation of momentum in radial direction

$$\begin{aligned}&\frac{\partial}{\partial t}(\rho V_r)+\frac{1}{r^2}\frac{\partial}{\partial r}(r^2\rho V_r^2)+\frac{1}{r\sin\theta}\frac{\partial}{\partial\theta}(\rho V_\theta V_r\sin\theta)-\frac{\rho V_\theta^2}{r}\\&\quad=-\frac{\partial P_d}{\partial r}+\rho g_r+\frac{1}{r^2}\frac{\partial}{\partial r}(r^2\tau_{rr})\\&\qquad+\frac{1}{r\sin\theta}\frac{\partial}{\partial\theta}(\tau_{r\theta}\sin\theta)-\frac{\tau_{\theta\theta}+\tau_{\phi\phi}}{r}\end{aligned} \tag{2}$$

Conservation of momentum in polar direction

$$\begin{aligned}&\frac{\partial}{\partial t}(\rho V_\theta)+\frac{1}{r^2}\frac{\partial}{\partial r}(r^2\rho V_r V_\theta)+\frac{1}{r\sin\theta}\frac{\partial}{\partial\theta}(\rho V_\theta^2\sin\theta)\\&\quad=-\frac{1}{r}\frac{\partial P_d}{\partial\theta}+\rho g_\theta+\frac{1}{r^3}\frac{\partial}{\partial r}(r^3\tau_{r\theta})\\&\qquad+\frac{1}{r\sin\theta}\frac{\partial}{\partial\theta}(\tau_{\theta\theta}\sin\theta)-\frac{\tau_{\phi\phi}\cot\theta}{r}\end{aligned} \tag{3}$$

where

$$\begin{aligned}\tau_{rr}&=\mu\left[2\frac{\partial V_r}{\partial r}-\frac{2}{3}\nabla\cdot\vec{V}\right]\\\tau_{\theta\theta}&=\mu\left[2\left(\frac{1}{r}\frac{\partial V_\theta}{\partial\theta}+\frac{V_r}{r}\right)-\frac{2}{3}\nabla\cdot\vec{V}\right]\\\tau_{\phi\phi}&=\mu\left[2\left(\frac{V_r}{r}+\frac{V_\theta\cot\theta}{r}\right)-\frac{2}{3}\nabla\cdot\vec{V}\right]\\\tau_{r\theta}&=\mu\left[r\frac{\partial}{\partial r}\left(\frac{V_\theta}{r}\right)+\frac{1}{r}\frac{\partial V_r}{\partial\theta}\right]\end{aligned} \tag{4}$$

and

$$\nabla\cdot\vec{V}=\frac{1}{r^2}\frac{\partial}{\partial r}(r^2V_r)+\frac{1}{r\sin\theta}\frac{\partial}{\partial\theta}(V_\theta\sin\theta) \tag{5}$$

Conservation of species

$$\begin{aligned}&\frac{\partial}{\partial t}(\rho Y_1)+\frac{1}{r^2}\frac{\partial}{\partial r}(\rho r^2 V_r Y_1)+\frac{1}{r\sin\theta}\frac{\partial}{\partial\theta}(\rho V_\theta\sin\theta Y_1)\\&\quad=\frac{1}{r^2}\frac{\partial}{\partial r}\left(\rho r^2 D_{12}\frac{\partial Y_1}{\partial r}\right)+\frac{1}{r\sin\theta}\frac{\partial}{\partial\theta}\left(\frac{1}{r}\rho\sin\theta D_{12}\frac{\partial Y_1}{\partial\theta}\right)\end{aligned} \tag{6}$$

Conservation of energy

$$\begin{aligned}&c_p\left[\frac{\partial}{\partial t}(\rho T)+\frac{1}{r^2}\frac{\partial}{\partial r}(r^2\rho T V_r)+\frac{1}{r\sin\theta}\frac{\partial}{\partial\theta}(\rho T V_\theta\sin\theta)\right]\\&\quad+(h_1-h_2)\left[\frac{\partial}{\partial t}(\rho Y_1)+\frac{1}{r^2}\frac{\partial}{\partial r}(\rho r^2 V_r Y_1)\right.\\&\qquad\left.+\frac{1}{r\sin\theta}\frac{\partial}{\partial\theta}(\rho V_\theta\sin\theta Y_1)\right]=\frac{1}{r^2}\frac{\partial}{\partial r}\left(r^2k\frac{\partial T}{\partial r}\right)\\&\quad+\frac{1}{r\sin\theta}\frac{\partial}{\partial\theta}\left(\frac{k}{r}\sin\theta\frac{\partial T}{\partial\theta}\right)+\frac{1}{r^2}\frac{\partial}{\partial r}\left[\rho r^2 D_{12}\frac{\partial Y_1}{\partial r}(h_1-h_2)\right]\\&\quad+\frac{1}{r\sin\theta}\frac{\partial}{\partial\theta}\left[\frac{1}{r}\rho\sin\theta D_{12}\frac{\partial Y_1}{\partial\theta}(h_1-h_2)\right]\end{aligned} \tag{7}$$

In the above equations, t refers to the temporal variable, P_d is the motion pressure, T is the temperature and Y_1 is the fuel mass fraction. In the momentum equations, τ represents the viscous stress tensor where τ_{rr}, $\tau_{\theta\theta}$ and $\tau_{\phi\phi}$ are the normal stresses in radial, polar and azimuthal direction, respectively, $\tau_{r\theta}$ is the shear stress, and $\nabla\cdot\vec{V}$ is the divergence of the velocity vector. The buoyancy force is introduced in the momentum equations through g_r and g_θ, where $g_r=g\cos\theta$ and $g_\theta=g\sin\theta$ are the gravitational acceleration in the radial and polar directions, respectively. The properties, ρ, k, μ and c_p are the density, thermal conductivity, viscosity and specific heat at constant pressure of the mixture, D_{12} is the binary mass diffusion coefficient and h is the specific enthalpy. Subscript 1 indicates the vaporizing fuel, subscript 2 indicates the inert gas, and subscripts r and θ refer to radial and polar variables, respectively. The strength of the buoyancy effect is defined by the Grashof number, $Gr=((\bar{\rho}_s-\rho_\infty)R^3g)/\rho_\infty\nu_\infty^2$, where $\bar{\rho}_s$ is the average density of the gaseous mixture at the droplet surface, ν is the kinematic viscosity, and the subscript ∞ denotes the gas phase variables evaluated at the ambient conditions. The Grashof number is defined in terms of density difference rather than temperature difference. The Boussinesq approximations, which are inaccurate for large temperature differences [13], are not employed in this study.

The governing equations are subjected to the following initial and boundary conditions.

The initial conditions ($t=0$) are:

(*a*) *gas phase*

$$T=T_\infty;\quad P=P_\infty;\quad \rho=\rho_\infty;\quad P_d=Y_1=V_r=V_\theta=0 \tag{8}$$

(*b*) *liquid phase*

$$T=T_0;\quad \rho=\rho_0;\quad P_d=0;\quad Y_1=1;\quad V_r=V_\theta=0 \tag{9}$$

At $t=0$, the initial conditions correspond to a sudden introduction of a cold droplet into a hot, and

stagnant environment. There is no motion in both the gas and the liquid phases initially. Temperature and mass fraction of the fuel in the gas phase are defined by the ambient conditions while the liquid phase is prescribed with a temperature of T_0 and fuel mass fraction of unity. A step change in temperature and mass fraction are imposed at the droplet surface. Initially, the properties in the entire gas phase are evaluated at T_∞, P_∞ and $Y_1 = 0$ while in the liquid phase, the properties are evaluated at T_0 and $Y_1 = 1$. In Eqs. (8) and (9), ρ_∞ is the ambient density of the inert gas and ρ_0 is the initial density of the liquid fuel.

The boundary conditions are:

(*a*) *gas phase at the axis of symmetry* ($\theta = 0$ *or* π)

$$V_\theta = 0; \quad \frac{\partial V_r}{\partial \theta} = \frac{\partial Y_1}{\partial \theta} = \frac{\partial T}{\partial \theta} = \frac{\partial P_d}{\partial \theta} = 0 \tag{10}$$

far from the droplet ($r = r_\infty$)

$$\frac{\partial V_\theta}{\partial r} = 0 \tag{11}$$

the radial velocity (V_r) is extrapolated using the continuity equation.

for inflow conditions ($V_r|_\infty \leqslant 0$)

$$Y_1 = 0; \quad T = T_\infty; \quad P_d = 0 \tag{12}$$

and for outflow conditions ($V_r|_\infty > 0$)

$$\frac{\partial Y_1}{\partial r} = \frac{\partial T}{\partial r} = \frac{\partial P_d}{\partial r} = 0 \tag{13}$$

(*b*) *liquid phase at the axis of symmetry* ($\theta = 0$ *or* π)

$$V_\theta = 0; \quad \frac{\partial V_r}{\partial \theta} = \frac{\partial Y_1}{\partial \theta} = \frac{\partial T}{\partial \theta} = \frac{\partial P_d}{\partial \theta} = 0 \tag{14}$$

The above equations indicate no transfer of energy or mass across the axis of symmetry in both the gas and the liquid phase. As a result, the gradients of velocity, temperature, and mass fraction with respect to θ are equal to zero. At the gas phase free-stream boundary, the polar velocity is specified to have a zero gradient radially. Over the "inflow" portion of this boundary ($V_r|_\infty \leqslant 0$), temperature and fuel mass fraction are prescribed to have their ambient values, while at the "outflow" portion ($V_r|_\infty > 0$), a zero gradient with respect to the radial coordinate is used for temperature and mass fraction of the fuel.

At the droplet interface ($r = R(t)$), a distinctive liquid/gas interface exists. The radial and polar velocity components, temperature and mass flux at the gas/liquid interface are obtained by solving the following interface equations:

(*a*) *shear stress continuity*

$$\tau_{r\theta,\mathrm{g}} = \tau_{r\theta,\mathrm{l}} \tag{15}$$

(*b*) *tangential velocity continuity*

$$V_{\theta,\mathrm{g}} = V_{\theta,\mathrm{l}} \tag{16}$$

(*c*) *temperature continuity*

$$T_\mathrm{g} = T_\mathrm{l} \tag{17}$$

(*d*) *conservation of mass flux*

$$\dot{m}'' = \rho_\mathrm{g}(V_{r,\mathrm{g}} - \dot{R}) = \rho_\mathrm{l}(V_{r,\mathrm{l}} - \dot{R}) \tag{18}$$

(*e*) *conservation of droplet mass*

$$\dot{R} = -\frac{1}{2}\frac{1}{\bar{\rho}_\mathrm{l}}\left[\int_0^\pi \dot{m}'' \sin\theta \,\mathrm{d}\theta + \frac{1}{3}R\frac{\partial \bar{\rho}_\mathrm{l}}{\partial t}\right] \tag{19}$$

(*f*) *energy conservation*

$$\begin{aligned}&\left(\dot{m}'' Y_{1,g} - \rho_\mathrm{g} D_{12,\mathrm{g}} \frac{\partial Y_{1,\mathrm{g}}}{\partial r}\right)(h_{1,\mathrm{g}} - h_{1,\mathrm{l}}) \\ &\quad + \left(\dot{m}'' Y_{2,\mathrm{g}} - \rho_\mathrm{g} D_{12,\mathrm{g}} \frac{\partial Y_{2,\mathrm{g}}}{\partial r}\right)(h_{2,\mathrm{g}} - h_{2,\mathrm{l}}) \\ &\quad - k_\mathrm{g}\left[\frac{1}{r^2}\frac{\partial}{\partial r}(r^2 T_\mathrm{g})\right] + k_\mathrm{l}\left[\frac{1}{r^2}\frac{\partial}{\partial r}(r^2 T_\mathrm{l})\right] = 0\end{aligned} \tag{20}$$

(*g*) *species conservation*

$$\dot{m}''(Y_{1,\mathrm{g}} - Y_{1,\mathrm{l}}) - \rho_\mathrm{g} D_{12,\mathrm{g}} \frac{\partial Y_{1,\mathrm{g}}}{\partial r} + \rho_\mathrm{l} D_{12,\mathrm{l}} \frac{\partial Y_{1,\mathrm{l}}}{\partial r} = 0 \tag{21}$$

In the above equations, subscripts g and l indicate variables in the gas side and liquid side at the droplet interface, respectively. $\dot{R}$ is the regression rate of the droplet surface, R is the instantaneous radius of the fuel droplet and $\dot{m}''$ is the mass flux at the droplet surface. The mass fraction of fuel at the interface is obtained by solving the vapor–liquid equilibrium relationships. The formulation in Williams [14] is used to derive the interface equations.

In addition to the above equations, the Peng–Robinson equation of state [15] is employed to model the real gas effects at high pressures and predict vapor–liquid equilibrium composition at the droplet surface. It has been shown by Jia and Gogos [16] and more recently by Zhu and Aggarwal [17] that among cubic equations of state, the Peng–Robinson equation predicts most accurately vapor–liquid equilibrium experimental data for hydrocarbons such as *n*-hexane [16] and *n*-heptane [17]. The Peng–Robinson equation of state is given in the form:

$$P = \frac{R_u T}{\upsilon - b} - \frac{a}{\upsilon(\upsilon + b) + b(\upsilon - b)} \tag{22}$$

where υ is the specific volume of the gaseous mixture, R_u is the universal gas constant, and a and b are the composition dependent parameters which are obtained by the mixing rules proposed in [15].

The vapor–liquid equilibrium relationships, critical state for binary systems and energy required for change of phase are obtained as described in detail in Jia and Gogos [16] and in Soh [18].

Transport and thermodynamic properties are calculated based on the methods recommended by Reid, Prausnitz and Polling [19]. The gas phase properties vary with temperature, pressure and composition while the liquid phase properties vary with temperature and composition only. Detailed presentation of transport and thermodynamic properties used can also be found in [16] and [18].

4. Numerical methods

The governing equations (both for the gas and the liquid phase) are solved in dimensionless form. The basic non-dimensionalization parameters used are initial droplet radius (R_0), diffusion velocities of the gas phase ($(v_\infty/R_0)\sqrt{Gr_0}$) and the liquid phase ($(v_0/R_0)\sqrt{Gr_0}$), diffusion times of the gas phase ($(R_0^2/v_\infty)(1/\sqrt{Gr_0})$) and the liquid phase ($(R_0^2/v_0)(1/\sqrt{Gr_0})$), and characteristic pressures of the gas phase ($Gr_0\rho_\infty v_\infty^2/R_0^2$) and the liquid phase ($Gr_0\rho_0 v_0^2/R_0^2$). The corresponding transport and thermodynamic properties in these parameters are evaluated at ambient conditions for the gas phase and at initial conditions for the liquid phase. Gr_0 is the initial Grashof number defined as $Gr_0 = (\rho_{s,0} - \rho_\infty)R_0^3 g/\rho_\infty v_\infty^2$, where $\rho_{s,0}$ is the initial density of the gas phase at the droplet surface.

The governing equations are discretized in a spatial coordinate system given by $r'' = r/R$ in the liquid phase and by a transformed coordinate system $r' = r/R = e^{z'}$ in the gas phase, where $r'' \leqslant 1$ and $1 \leqslant r' \leqslant r_\infty$. The outer boundary of the computational domain in the radial direction is indicated as r_∞. In view of the above coordinate transformation, a constant step size $\Delta z'$ in the gas phase, results in the concentration of grid points near the droplet surface where the gradients are steep. A constant step size $\Delta r''$ is used in the liquid phase and a constant step size $\Delta\theta$ is used along the polar coordinate for both the gas and liquid phase. Typical step sizes used in the present analysis are: $\Delta z' = 3.2 \times 10^{-2}$, $\Delta r'' = 1.96 \times 10^{-2}$, $\Delta\theta = 2^\circ$ and $r_\infty = 33$. Obtained solutions are independent of grid sizes.

The momentum, mass and heat transfer solutions of droplet evaporation are obtained by solving the governing equations with the finite-volume (Patankar [20]) and SIMPLEC (Van Doormaal and Raithby [21]) methods. These methods are used to discretize the governing equations and boundary conditions in the computational domain. The discretized equations are solved by the ADI method with a TDMA solver being used along radial and polar directions. To avoid a decoupled or checkboard pressure field, the staggered mesh is also employed in the domain. All variables are solved iteratively within each time step using the following procedure. First, the transport and thermodynamic properties of the gas and the liquid phase are calculated based on the temperature, pressure and composition from the previous time step or iteration. Then, the droplet surface quantities $V_{r,g}$, $V_{\theta,g}$, T_s, $\dot{R}$, $Y_{1,g}$ and $\dot{m}''$ are obtained by solving Eqs. (15)–(21). Next, the composition and temperature of both phases are solved using Eqs. (6) and (7) and the relevant boundary conditions given by Eqs. (10)–(14). The motion pressure, radial velocity and polar velocity of the gas and liquid phase are then solved using Eqs. (1)–(3) and the SIMPLEC scheme with a staggered mesh. All the calculations are performed iteratively within a time step till the convergence criterion is fulfilled. The convergence criterion is defined as $|(\psi_{new} - \psi_{old})/(\psi_{old})| \leqslant 1 \times 10^{-4}$, where ψ represents the surface mass flux or temperature. Iterations within each time step are terminated when both quantities satisfy the convergence criterion. Subscripts new and old indicate the variables at the current and previous iteration, respectively. The calculations are terminated when the square of the dimensionless droplet diameter $(d/d_0)^2 < 0.2$, or when the critical state for the binary system is reached.

For the gas phase, a step function is used as an initial condition for temperature. Variable time steps are employed to improve the computing accuracy and efficiency. Obtained solutions are independent of the sizes of the time steps used. The total CPU time required for a solution ranged from less than 12 h (for high P_∞ and Gr) to approximately 40 h (for low P_∞ and Gr) on a Sun Ultra Enterprise 3000 server.

5. Results and discussion

Table 1 shows all cases considered by Matlosz et al. [9] in their experimental study of a *n*-hexane droplet evaporating within a high pressure nitrogen environment. P_∞ is the ambient pressure, T_0 is the initial droplet temperature and d_0 is the initial droplet diameter. The experiment was conducted under normal gravity and the ambient temperature T_∞ was maintained at 548 K at all times.

Table 1
Conditions for droplet evaporation in the experiments of Matlosz et al.

Case #	P_∞ (atm)	T_0 (K)	d_0 (μm)
1	6.8	329	820
2	20.4	346	700
3	40.8	366	880
4	81.6	353	800
5	102.0	361	860

Figs. 2 and 3 show the time histories of the dimensionless droplet diameter squared and the corresponding droplet temperature for cases 1, 2, 4, and 5 of Table 1. Both numerical and experimental results are presented. At ambient pressures of 6.8 atm (Fig. 2(a) and (b)) and 20.4 atm (Fig. 2(c) and (d)), the comparisons with the experimental results of Matlosz et al. are very good. The measured droplet wet-bulb temperature is about 10 °C above the one predicted with the numerical model. Heat conduction along the wire of the chromel–alumel thermocouple (50 μm in diameter) that was used to support the droplet and to measure its temperature may be the main cause for the above difference between measured and predicted droplet wet-bulb temperature. The lower droplet lifetimes measured by Matlosz et al. compared to the present predictions (see Fig. 2) may then be a result of the energy pumped at the center of the droplet through the thermocouple wire. At the high ambient pressures of 81.6 atm (Fig. 3(a) and (b)) and 102.0 atm (Fig. 3(c) and (d)), the experimentally measured droplet lifetime and droplet temperature deviate significantly from the numerical predictions. The surface tension decreases with increasing pressure, causing the droplet shape in the experiment to deviate from spherical and to become increasingly more ellipsoidal with increasing pressure (the present model assumes spherical droplet shape). A change from a spherical to an ellipsoidal geometry increases both the droplet surface area and the characteristic length resulting in a larger "experimental" Grashof number. The increased droplet surface area and the increased Grashof number both enhance the evaporation rate, leading to additional reasons (beyond heat conduction through the thermocouple wire) for droplet lifetime shortening.

The predicted temporal variation of the droplet diameter squared, $(d/d_0)^2$, for cases 1 and 5 of Table 1 are shown in Fig. 4 both for normal and microgravity. Microgravity is simulated numerically by setting the acceleration due to gravity negligibly small ($g = 9.81 \times 10^{-6}$ m/s). Under microgravity conditions, the droplet lifetimes predicted by the model are close to each other for the two cases presented in Fig. 4, in spite of the widely different pressures considered. This is in agreement with Jia and Gogos [16] who have shown in their numerical study that for ambient temperatures close to the critical temperature of the fuel ($T_c = 507$ K for *n*-hexane) the droplet lifetime is insensitive to pressure over a very wide range. This result was later confirmed

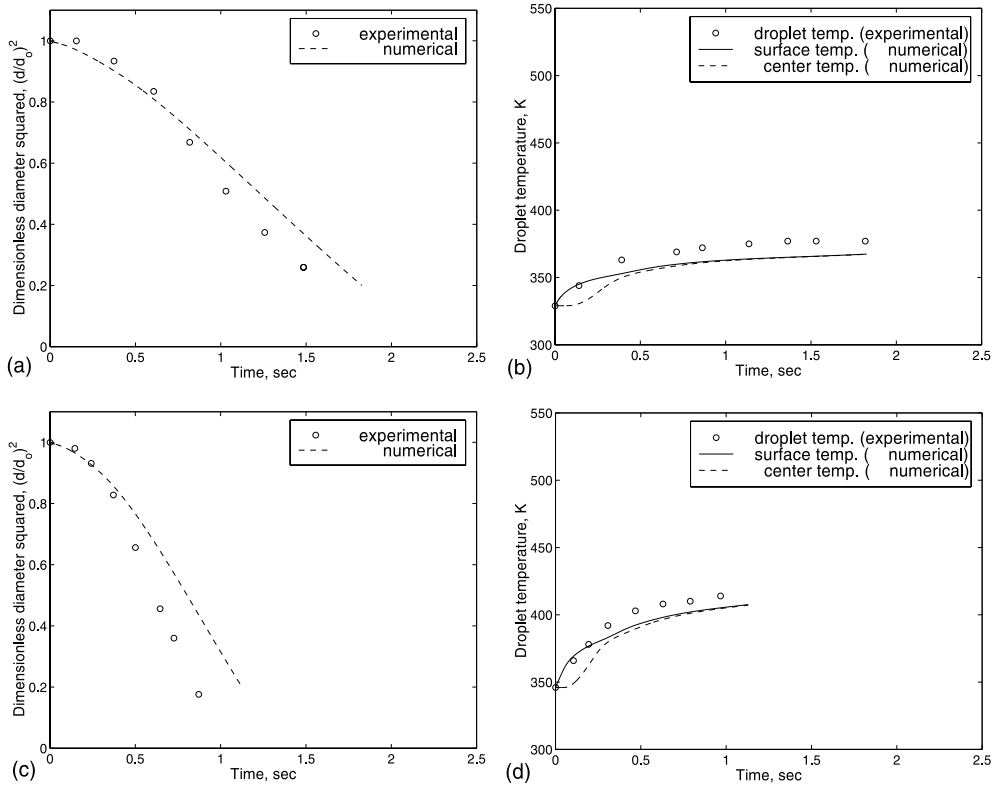

Fig. 2. Comparison of the numerical results to the experimental measurements of Matlosz et al. [9]: temporal variation of dimensionless droplet diameter squared and droplet temperature ($T_\infty = 548$ K, cases 1 and 2). Case 1: $P_\infty = 6.8$ atm (a, b); case 2: $P_\infty = 20.4$ atm (c, d).

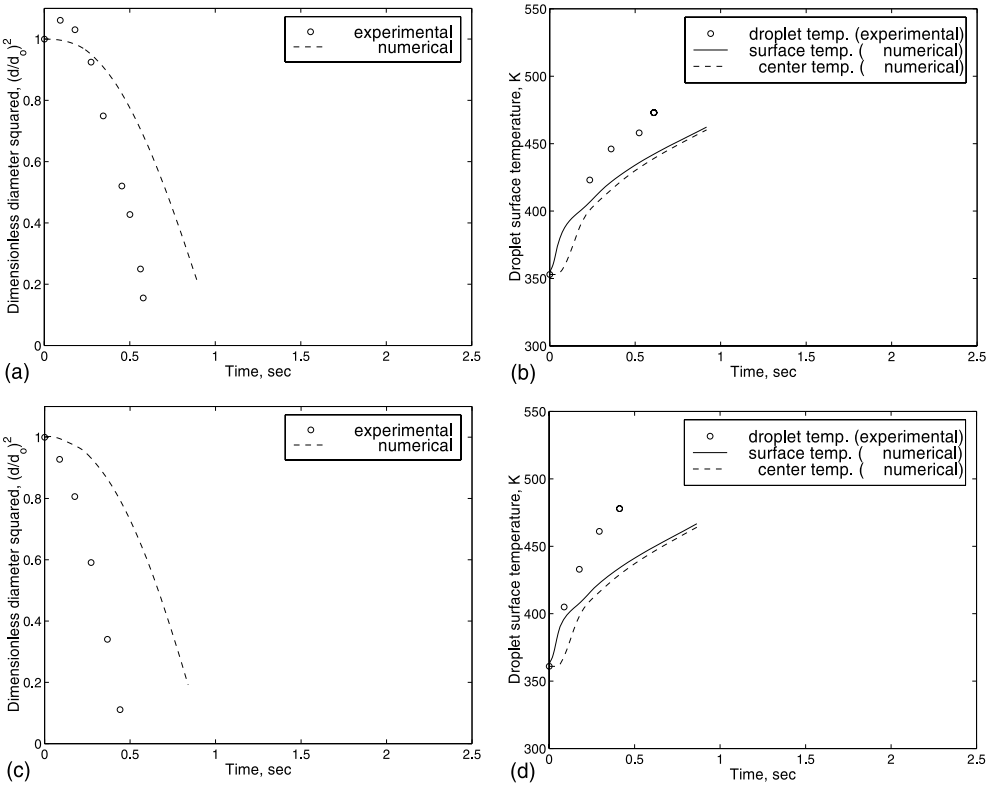

Fig. 3. Comparison of the numerical results to the experimental measurements of Matlosz et al. [9]: temporal variation of dimensionless droplet diameter squared and droplet temperature ($T_\infty = 548$ K, cases 4 and 5). Case 4: $P_\infty = 81.6$ atm (a, b); case 5: $P_\infty = 102.0$ atm (c, d).

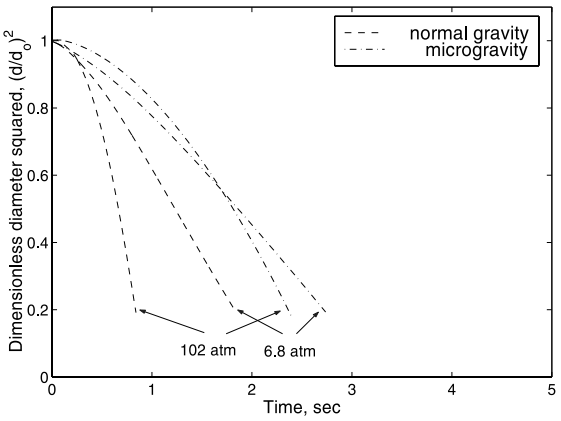

Fig. 4. Predicted temporal variation of the droplet diameter squared for cases 1 and 5 of Table 1, both for normal and microgravity.

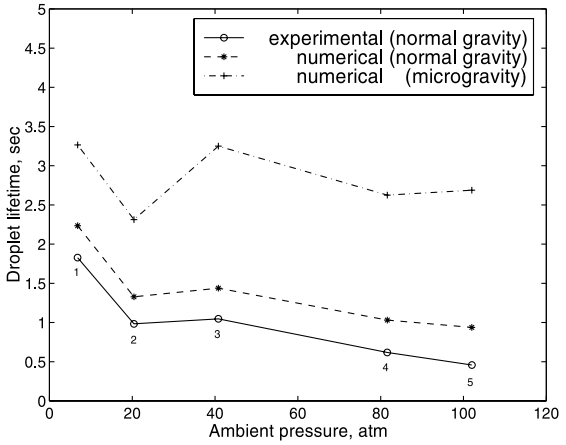

Fig. 5. Comparison of experimental (Matlosz et al. [9]) and numerical (present study) results for droplet evaporation with ambient pressure. Numbers on the curves indicate cases presented on Table 1.

experimentally by Nomura et al. [22] and numerically by Zhu and Aggarwal [17]. Under normal gravity conditions, however, natural convection causes a decrease in the droplet lifetime, which becomes more dominant with increasing ambient pressure.

Fig. 5 presents droplet lifetime results and compares numerical predictions (both normal and microgravity) against the experimental data of Matlosz et al. [9]. The

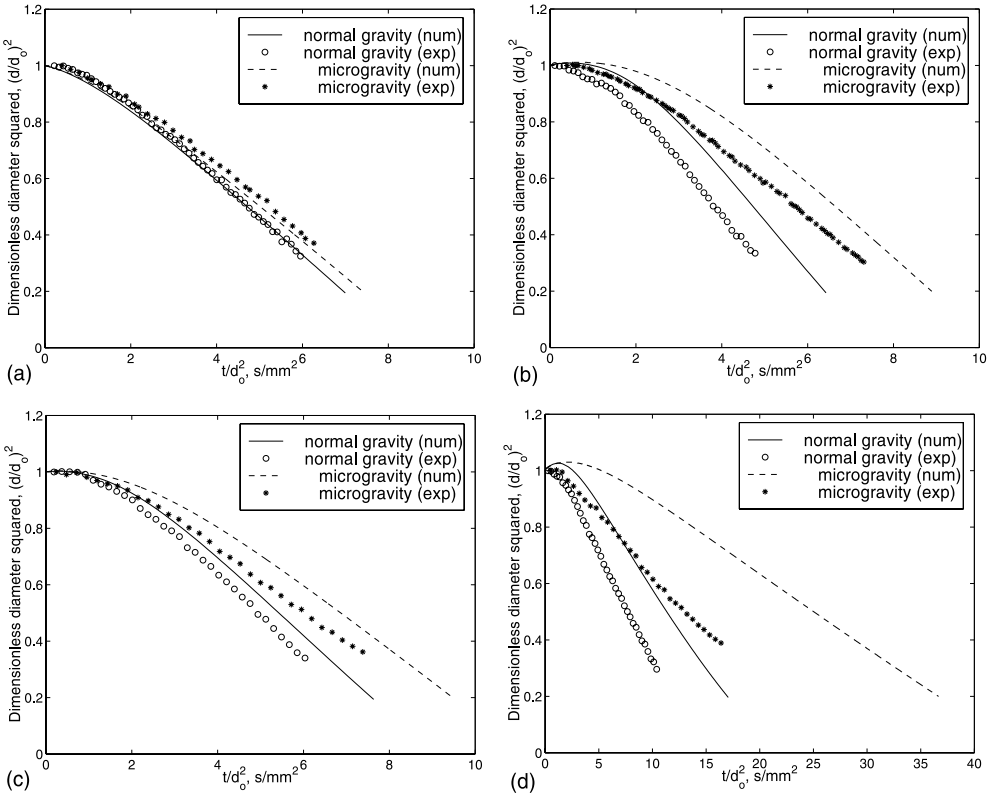

Fig. 6. Comparison of experimental (Nomura et al. [10]) and numerical (present study) results under both normal and microgravity conditions. (a) $T_\infty = 448$ K, $P_\infty = 0.1$ MPa, $d_0 = 608$ μm (normal gravity), $d_0 = 634$ μm (microgravity). (b) $T_\infty = 450$ K, $P_\infty = 0.5$ MPa, $d_0 = 604$ μm (normal gravity), $d_0 = 748$ μm (microgravity). (c) $T_\infty = 474$ K, $P_\infty = 1.0$ MPa, $d_0 = 607$ μm (normal gravity), $d_0 = 783$ μm (microgravity). (d) $T_\infty = 398$ K, $P_\infty = 5.0$ MPa, $d_0 = 698$ μm (normal gravity), $d_0 = 710$ μm (microgravity).

open circles ($\circ$) indicate the experimental data (obtained under normal gravity conditions), the asterisks ($*$) show the numerical predictions under normal gravity and the crosses ($+$) represent the numerical predictions under microgravity. As shown in the figure, the normal gravity predictions are in good agreement with the experimental data both at low and moderate pressures. The model predictions deviate from the experimental data with increasing pressure. At the highest ambient pressure considered ($P_\infty = 102$ atm), the model overpredicts the droplet lifetime by a factor of 2, for reasons that were discussed earlier. Fig. 5 also presents microgravity predictions employing the present model. The effect of natural convection on the droplet lifetime becomes more dominant with increasing ambient pressure as the Grashof number changes from $\sim O(10^1)$ at the lowest to $\sim O(10^3)$ at the highest pressure considered. At the highest ambient pressure considered ($P_\infty = 102$ atm), natural convection decreases the droplet lifetime by a factor of 3.

Numerical predictions using the present model are also compared with results obtained in the recent experiment conducted by Nomura et al. [10]. The experiment involved the evaporation of a cold *n*-heptane droplet in a hot air environment under normal or microgravity conditions. The initial droplet temperature is 300 K and the ambient temperature is below the critical temperature of the fuel. The initial droplet diameter is in the range of 0.6–0.8 mm.

Fig. 6 shows the dimensionless droplet diameter squared as a function of time for $P_\infty = 0.1$, 0.5, 1.0 and 5.0 MPa. Numerical predictions are compared to the experimental data of Nomura et al. [10], both for normal and microgravity conditions. The numerical predictions deviate from the experimental data with increasing ambient pressure. It has been shown by Gogos and Zhang [23] that the introduction of the droplet in the test position is the main reason for the difference between the numerical and the experimental results. [1] The study by

[1] Nomura et al. [10] employed a silica fiber for droplet suspension, whose thermal conductivity is almost two orders of magnitude smaller than the chromel–alumel thermocouple suspender used by Matlosz et al. [9]. Heat conduction through the suspender in Nomura et al. [10] is therefore negligible.

Table 2
Initial Reynolds numbers for microgravity cases in Fig. 6

d_0 (μm)	T_∞ (K)	P_∞ (MPa)	μ_∞/ρ_∞ (m^2/s)	Re_0
634	448	0.1	3.127×10^{-5}	7.60
748	450	0.5	6.314×10^{-6}	44.4
783	474	1.0	3.458×10^{-6}	84.9
710	398	5.0	5.329×10^{-7}	499.6

Nomura et al. [10] aimed to provide data for stationary droplets evaporating within a stagnant microgravity or within a normal gravity environment. However, as reported in [10,24], the droplet was moved from the droplet generator to the test position (a length of 60 mm) in 0.16 s within the hot nitrogen environment. This process introduced droplet motion at an average velocity of 0.375 m/s for 0.16 s. During this period, the droplet experienced considerable heat-up. In addition, the shear stress at the liquid/gas interface introduced circulation within the droplet interior. Table 2 presents the initial Reynolds number Re_0 ($Re_0 = \rho_\infty U_{\infty,0} d_0/\mu_\infty$) where $U_{\infty,0} = 0.375$ m/s, d_0 is the initial droplet diameter and ρ_∞ and μ_∞ are the density and absolute viscosity evaluated at ambient conditions. The experimental and numerical results for microgravity are very close to each other in Fig. 6(a), which corresponds to low pressure (0.1 MPa). At this low pressure, as shown in Table 2, the initial Reynolds number is only 7.60. With increasing pressure, the gas phase becomes more dense and, mostly due to this, the initial Reynolds number increases. The increasing strength of convection is the cause for the increasing deviation of the experimental data from the numerical predictions with increasing ambient pressure. The numerical model developed by Gogos and Zhang [23] for moving droplets while evaporating within a high pressure nitrogen environment can easily simulate the droplet motion and associated internal circulation as well as internal circulation that is sustained beyond the initial 0.16 s. It has been shown by Gogos and Zhang [23] [2] that when this effect is included, the agreement between the microgravity experimental data and the numerical results is excellent. The same effect could be the main reason for the difference shown in Fig. 6 between the experimental and numerical results at normal gravity. Harstad and Bellan [25] have also reported similar differences between their predictions for spherically symmetric droplet evaporation and the microgravity experimental data of Nomura and his co-workers.

The experimentally validated axisymmetric numerical model has been used to conduct a parametric study to further examine the effect of natural convection and ambient pressure on droplet evaporation. Ambient pressures are varied from 1 to 100 atm for normal or microgravity conditions for a *n*-heptane droplet evaporating within a nitrogen environment. The initial droplet diameter is 800 μm (unless otherwise indicated), the initial droplet temperature is 300 K, and the ambient temperature is 800 K.

The gas phase temperature, streamline and fuel mass fraction contours at different times are shown in Figs. 7–9 for a "typical" solution under normal gravity conditions ($P_\infty = 60$ atm, $T_\infty = 800$ K, $T_0 = 300$ K and $d_0 = 800$ μm). Results are presented for $t = 0.0079$, 0.058, 0.11, 0.21, 0.40 and 0.61 s and the predicted droplet lifetime is 0.75 s. Initially, there is no relative motion between the cold fuel droplet and the hot ambient gas. Therefore, very early in the droplet lifetime the temperature contours are radially symmetric ($t = 0.0079$ s, Fig. 7), since conduction is the dominant mode of heat transfer, and the fuel mass fraction contours are radially symmetric ($t = 0.0079$ s, Fig. 9) as the fuel diffuses radially outward from the droplet surface. However, even at this early time, a weak axisymmetric vortex is formed near the droplet ($t = 0.0079$ s, Fig. 8). As time progresses, the buoyancy-induced motion intensifies and the vortex moves downward and eventually out of the computational domain (Fig. 8). Similarly, both the fuel mass fraction contours (Fig. 9) and the temperature contours (Fig. 7) change from radially symmetric, to an "egg" shape, and eventually to a downward moving plume.

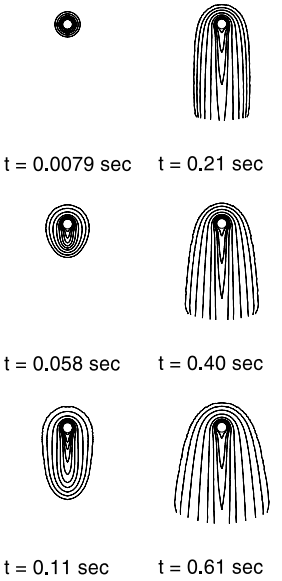

Fig. 7. Gas phase temperature contours under normal gravity conditions at different times ($P_\infty = 60$ atm, $T_\infty = 800$ K, $T_0 = 300$ K and $d_0 = 800$ μm).

[2] The present model in the limit of negligibly small gravity is in excellent agreement with the axisymmetric model of Gogos and Zhang [23] in the limit of negligibly small Reynolds number.

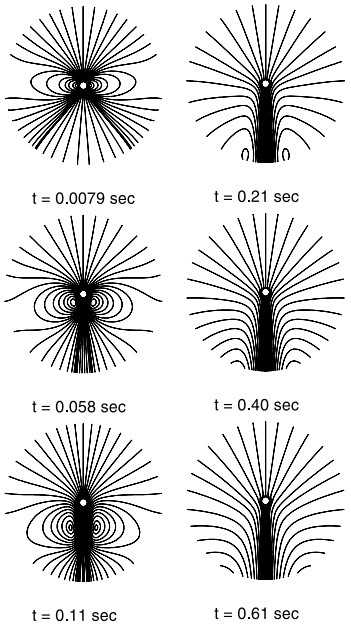

Fig. 8. Gas phase stream function contours under normal gravity conditions at different times ($P_\infty = 60$ atm, $T_\infty = 800$ K, $T_0 = 300$ K and $d_0 = 800$ μm).

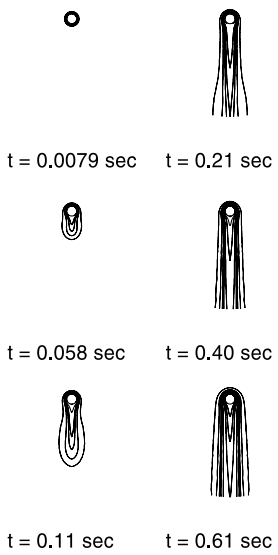

Fig. 9. Gas phase fuel mass fraction contours under normal gravity conditions at different times ($P_\infty = 60$ atm, $T_\infty = 800$ K, $T_0 = 300$ K and $d_0 = 800$ μm).

Fig. 10(a) shows the temporal variation of dimensionless droplet diameter squared for ambient pressures of 10, 30, 60 and 100 atm. During the early period of evaporation, the droplet swells due to the initial heat-up of the droplet interior, and the dimensionless droplet

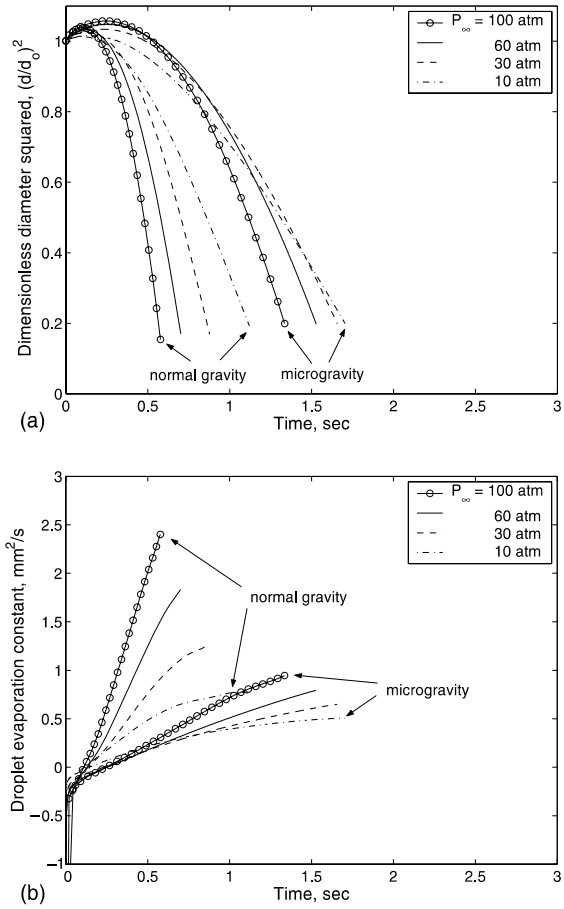

Fig. 10. Temporal variation of (a) dimensionless droplet diameter squared and (b) droplet evaporation constant at normal and microgravity for various ambient pressures.

diameter squared assumes values above unity. The droplet swelling and the heat-up period are more dominant in the absence of gravity. The lifetime of the droplet decreases with increasing ambient pressure. Comparison of normal gravity and microgravity results indicates that the effect of natural convection on droplet evaporation is very important in the cases considered. The enhancement in the rate of droplet evaporation by natural convection becomes more significant as ambient pressure increases. The droplet lifetime under normal gravity conditions decreases with ambient pressure more significantly than it decreases under microgravity.

Fig. 10(b) presents the time histories of the droplet evaporation constant (K), defined as $K = -(\mathrm{d}/\mathrm{d}t)(d^2)$. It is shown that K increases with time throughout the droplet lifetime. The higher the ambient pressure, the steeper the change in K. Under normal gravity conditions, the higher the ambient pressure, the stronger the buoyancy-induced flow, causing a steeper increase in the evaporation constant with time. This, for example, leads

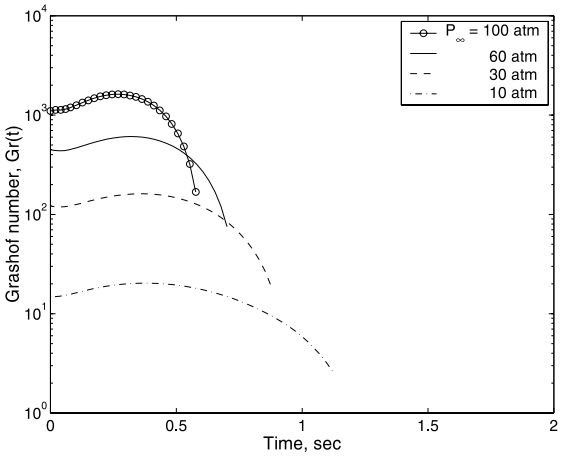

Fig. 11. Temporal variation of Grashof number under normal gravity conditions for various ambient pressures.

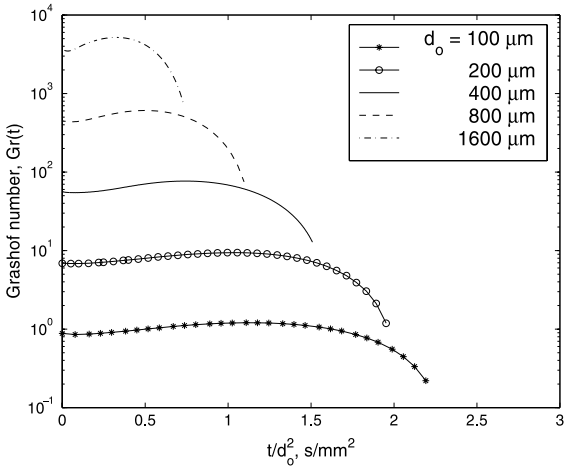

Fig. 13. Temporal variation of Grashof number under normal gravity conditions for different initial droplet diameters and $P_\infty/P_c = 2.2$.

to a very steep increase in K with time for the highest pressure considered ($P_\infty = 100$ atm).

Fig. 11 examines the effect of ambient pressure on Grashof number under normal gravity conditions. The strength of natural convection over an 800 μm evaporating droplet increases as Grashof number changes from $\sim O(10^1)$ at $P_\infty = 10$ atm to $\sim O(10^3)$ at $P_\infty = 100$ atm. The higher the ambient pressure, the closer the Grashof number remains to its initial value throughout most of the droplet lifetime because of the droplet swelling and heat-up of the droplet interior.

The droplet lifetime as a function of ambient pressure, for droplets of various sizes, is plotted in Fig. 12, both under microgravity and normal gravity conditions. Under microgravity, the droplet lifetime (t_e/d_0^2) decreases gradually with increasing pressure. The initial droplet size, d_0, is eliminated from the problem on scaling time with respect to d_0^2. Hubbard et al. [26] showed this to be true at low ambient pressures (1–10 atm). The present work extends this result to ambient pressures about 3.5 times the critical pressure of the fuel. Under normal gravity conditions, the droplet lifetime decreases with increasing ambient pressure, however, as expected, the initial droplet size is not eliminated from the problem on scaling time with respect to d_0^2. The larger the droplet diameter, the more significant the reduction in droplet lifetime with increasing ambient pressure, especially at relatively small pressures ($P_\infty/P_c < 0.5$). Fig. 12 also shows that, for a spray-droplet of typical size (say, $d_0 = 100$ μm), natural convection is negligible at the lowest ambient pressures considered, and remains insignificant even at the highest pressures considered.

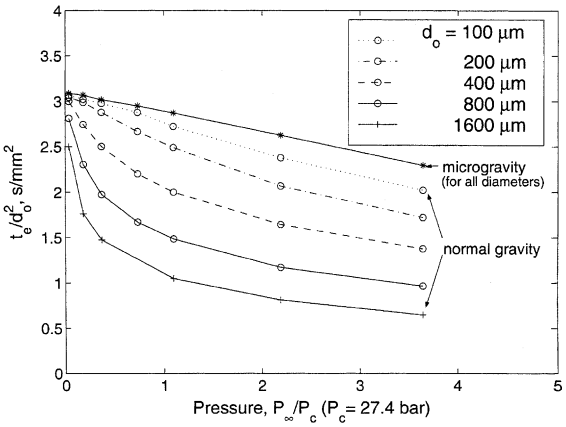

Fig. 12. Droplet lifetime (t_e/d_0^2) at different ambient pressures for five different initial droplet diameters.

Fig. 13 examines the effect of initial droplet diameter on Grashof number under normal gravity conditions for $P_\infty/P_c = 2.2$. The strength of natural convection over an evaporating droplet increases as Grashof number changes from $\sim O(10^0)$ for $d_0 = 100$ μm to $\sim O(10^3)$ for $d_0 = 1600$ μm. For the droplet sizes considered, Grashof number remains very close to its initial value throughout most of the droplet lifetime because of the droplet swelling and the droplet interior heat-up.

6. Conclusions

An axisymmetric numerical model has been developed to study fuel droplet evaporation in a normal or a microgravity environment over a wide range of ambient pressures. Variable properties in the gas and liquid

phase, real gas effects on the heat of vaporization and the vapor–liquid equilibrium condition at the droplet interface, solubility of the inert species into the liquid phase and liquid phase internal circulation are all considered. The transient gas and liquid phase equations of mass, species, momentum and energy conservation are solved using the finite volume and SIMPLEC methods. Predicted results are in good agreement with low pressure experimental data available in the literature. Explanations have been provided for the deviation between experimental data and numerical predictions at high pressures. The model predictions show that: (a) Under microgravity conditions, the initial droplet size, d_0, is eliminated from the problem on scaling time with respect to d_0^2 over the entire pressure range considered (1–100 atm). (b) The droplet lifetime under normal gravity conditions decreases with ambient pressure more significantly than it decreases under microgravity. (c) Under normal gravity conditions, the larger the droplet diameter, the more significant the reduction in droplet lifetime with increasing ambient pressure, especially at relatively small pressures ($P_\infty/P_c < 0.5$). (d) Under normal gravity conditions, the higher the ambient pressure, the stronger the effect of natural convection, causing a steeper increase in the droplet surface temperature and the evaporation constant with time. (e) For a spray-droplet of typical size (say, $d_0 = 100$ μm), natural convection is negligible at the lowest ambient pressures considered, and remains insignificant even at the highest pressures considered. (f) The higher the ambient pressure, the closer the Grashof number remains to its initial value throughout most of the droplet lifetime because of the droplet swelling and the heat-up of the droplet interior.

Acknowledgements

This research was funded by NASA EPSCoR under Grant No. NCC5-169 and ARO EPSCoR under Grant No. DAAD19-99-1-0116. The support is greatly appreciated. The authors are also grateful to Dr. Hiroshi Nomura for providing the experimental data for comparison. Computational resources were provided by the Thermal/Fluids Computational Facility and the Research Computing Facility at the Unversity of Nebraska-Lincoln. The authors are thankful to one of the reviewers whose comments improved the paper.

References

[1] A.H. Lefebvre, Gas Turbine Combustion, Hemisphere Publishing Corporation, New York, 1983, pp. 157–178.

[2] S.D. Givler, J. Abraham, Supercritical droplet vaporization and combustion studies, Prog. Energy Combust. Sci. 22 (1996) 1–28.

[3] W. Sirignano, in: Fluid Dynamics and Transport of Droplets and Sprays, Cambridge University Press, Cambridge, UK, 1999, pp. 258–270.

[4] J. Bellan, Supercritical (and subcritical) fluid behavior and modeling: drops, streams, shear, and mixing layers, jets and sprays, Prog. Energy Combust. Sci. 26 (4–6) (2000) 329–366.

[5] H.S. Lee, A.C. Fernandez-Pello, G.M. Corcos, A.K. Oppenheim, A mixing and deformation mechanism for a supercritical fuel droplet, Combust. Flame 81 (1990) 50–58.

[6] R.J. Litchford, S.M. Jeng, LOX vaporization in high-pressure hydrogen-rich gas, AIAA 26th Joint Propulsion Conference, Orlando, FL, 1990, no. AIAA 90-2191.

[7] J.P. Delplanque, W.A. Sirignano, Numerical study of the transient vaporization of an oxygen droplet at sub- and super-critical conditions, Int. J. Heat Mass Transfer 36 (1993) 303–314.

[8] J.P. Delplanque, W.A. Sirignano, Boundary layer stripping effects on droplet transcritical convective vaporization, Atomization Sprays 4 (1994) 325–349.

[9] R.L. Matlosz, S. Leipziger, T.P. Torda, Investigation of liquid drop evaporation in a high temperature and high pressure environment, Int. J. Heat Mass Transfer 15 (1972) 831–852.

[10] H. Nomura, H. Rath, J. Sato, M. Kono, Effects of ambient pressure and natural convection on fuel droplet evaporation, 4th Asian-Pacific International Symposium on Combustion and energy Utilization, 1997, pp. 266–271.

[11] G. Gogos, S.H. Soh, Sub- and super-critical droplet evaporation within a natural convection environment, First Joint Meeting of the US Sections of the Combustion Institute, Washington DC, 1999, pp. 284–287.

[12] G. Gogos, S.H. Soh, Effects of gravity and ambient pressure on liquid fuel droplet evaporation, Proceedings of the 2000 Technical Meeting of the Central States Section of the Combustion Institute, Indianapolis, IN, 2000, pp. 359–364.

[13] D. Gray, A. Giorgini, The validity of the Boussinesq approximation for liquids and gases, Int. J. Heat Mass Transfer 19 (1976) 545–551.

[14] F.A. Williams, in: Combustion Theory, second ed., The Benjamin/Cummings Publishing Company, Menlo Park, California, 1985, pp. 13–17.

[15] D.Y. Peng, D.B. Robinson, A new two-constant equation of state, Ind. Eng. Chem. Fund. 15 (1976) 59–64.

[16] H. Jia, G. Gogos, High pressure droplet vaporization; effects of liquid-phase gas solubility, Int. J. Heat Mass Transfer 36 (1993) 4419–4431.

[17] G.S. Zhu, S.K. Aggarwal, Transient supercritical droplet evaporation with emphasis on the effects of equation of state, Int. J. Heat Mass Transfer 43 (2000) 1157–1171.

[18] S.H. Soh, Effects of gravity and ambient pressure on liquid fuel droplet evaporation, M.S. Thesis, University of Nebraska, Lincoln, NE, 2000.

[19] R.C. Reid, J.M. Prausnitz, B.E. Polling, The Properties of Gases and Liquids, fourth ed., McGraw-Hill, New York, 1987.

[20] S.V. Patankar, Numerical Heat Transfer and Fluid Flow, Hemisphere Publishing Corporation, New York, 1980.
[21] J.P. Van Doormaal, G.D. Raithby, Enhancements of the SIMPLE method for predicting incompressible fluid flows, Numer. Heat Transfer 7 (1984) 147–163.
[22] H. Nomura, Y. Ujiie, H. Rath, J. Sato, M. Kono, Experiment study on high pressure droplet evaporation using microgravity conditions, Proc. Combust. Inst. 26 (1996) 1267–1273.
[23] G. Gogos, H.T. Zhang, Evaporation of a spherical moving fuel droplet over a wide range of ambient pressures within a nitrogen environment, Proceedings of the 2000 Technical Meeting of the Central States Section of the Combustion Institute, Indianapolis, IN, 2000, pp. 353–358.
[24] R. Ristau, U. Nagel, H. Iglseder, J. Konig, H. Rath, H. Normura, M. Kono, M. Tanabe, J. Sato, Theoretical and experimental investigations on droplet evaporation and droplet ignition at high pressures, J. Microgravity Sci. Technol. 6 (1993) 223–228.
[25] K. Harstad, J. Bellan, An all-pressure fluid drop model applied to a binary mixture: heptane in nitrogen, Int. J. Multiphase Flow 26 (10) (2000) 1675–1706.
[26] G.L. Hubbard, V.E. Denny, A.F. Mills, Droplet Evaporation: effects of transients and variable properties, Int. J. Heat Mass Transfer 18 (1975) 1003–1008.